Bi-functional Interfaces by Poly-Ionic Liquid Treatment in Efficient *pin* and *nip* Perovskite Solar Cells

Pietro Caprioglio[a,b*], Daniel Saul Cruz[c], Sebastián Caicedo-Dávila[d], Fengshuo Zu[e], Albertus Adrian Sutanto[f], Francisco Peña-Camargo[a], Lukas Kegelmann[b], Daniele Meggiolaro[m], Luca Gregori[n], Christian M. Wolff [a], Burkhard Stiller[a], Lorena Perdigón-Toro[a], Hans Kobler[l], Bor Li[b], Emilio Gutierrez-Partida[a], Iver Lauermann[d], Antonio Abate[l], Norbert Koch[e], Filippo De Angelis[m,n,o], Bernd Rech[g], Giulia Grancini[f,i], Daniel Abou-Ras[d], Mohammad Khaja Nazeeruddin[f], Martin Stolterfoht[a], Steve Albrecht[b,h], Markus Antonietti[c] and Dieter Neher[a*]

[a] Institute of Physics and Astronomy, University of Potsdam, 14476 Potsdam, Germany
[b] Young Investigator Group Perovskite Tandem Solar Cells, Helmholtz-Zentrum Berlin für Materialien und Energie GmbH, 12489 Berlin, Germany
[c] Max Planck Institute of Colloids and Interfaces, Am Mühlenberg 1, 14476 Potsdam, Germany
[d] Helmholtz Zentrum Berlin für Materialien und Energie GmbH, 12489 Berlin, Germany
[e] Humboldt University, Institut f¨ur Physik, Newtonstraße 15, 12489 Berlin, Germany
[f] Group for Molecular Engineering of Functional Materials, Institute of Chemical Sciences and Engineering, École Polytechnique Fédérale de Lausanne, CH-1951 Sion, Switzerland
[g] Institute for Silicon Photovoltaics, Helmholtz-Zentrum Berlin für Materialien und Energie GmbH, 12489 Berlin, Germany
[h] Faculty IV – Electrical Engineering and Computer Science Technical, University Berlin, 10587 Berlin, Germany
[i] Department of Chemistry, University of Pavia, Via Torquato Taramelli 14, 27100 Pavia, Italy
[l] Young Investigator Group Active Materials and interfaces for stable perovskite solar cells Helmholtz-Zentrum Berlin für Materialien und Energie GmbH, 12489 Berlin, Germany
[m] Computational Laboratory for Hybrid/Organic Photovoltaics (CLHYO), Istituto CNR di Scienze e Tecnologie Chimiche "Giulio Natta" (CNR-SCITEC), Via Elce di Sotto 8, 06123 Perugia, Italy
[n] Department of Chemistry, Biology and Biotechnology, University of Perugia, Perugia, Italy
[o] CompuNet, Istituto Italiano di Tecnologia, Via Morego 30, 16163 Genova, Italy

Corresponding author: neher@uni-potsdam.de, capriogl@uni-potsdam.de

Abstract

Approaches to boost the efficiency and stability of perovskite solar cells often address one singular problem in a specific device configuration. In this work, we utilize a poly(ionic-liquid) (PIL) to introduce a multi-functional interlayer to improve the device efficiency and stability for different perovskite compositions and architectures. The presence of the PIL at the perovskite surface reduces the non-radiative losses down to 60 meV already in the neat material, indicating effective surface trap passivation, thereby pushing the external photoluminescence quantum yield up to 7%. In devices, the PIL treatment induces a bi-functionality of the surface where insulating areas act as a blocking layer reducing interfacial charge recombination and increasing the V_{OC}, whereas, at the same time, the passivated neighbouring regions provide more efficient charge extraction, increasing the *FF*. As the result, these solar cells exhibit outstanding V_{OC} and FF values of 1.17 V and 83% respectively, with the best devices reaching conversion efficiencies up to 21.4%. The PIL-treated devices additionally show enhanced stability during maximum power point tracking (>700h) and unchanged efficiencies after 10 months of shelf storage. By applying the PIL to small and wide bandgaps perovskites and to *nip* cells, we corroborate the generality of this methodology to improve the efficiency in various cell architectures and perovskite compositions.

Introduction

In recent years, metal halide perovskites (MHPs) have gained a tremendous interest by the photovoltaics research community. This is due to their sky-rocketing power conversion efficiencies (PCE) (>25%), intriguing material properties[1–3] and promising low-cost production.[4,5] MPHs benefit from a high absorption coefficient, panchromatic absorption of light[6], long carrier diffusion length[7,8] and shallow trap energy levels.[1] The combination of these properties allows for a high photocurrent and low non-radiative recombination with high (external) photoluminescence yields (>20%).[9] Despite the tremendous improvements that this technology witnessed during the last decade[10], perovskite solar cells (PSCs) have not yet reached their theoretically predicted efficiencies[11] and still suffer from long-term stability issues.[12] In particular, *pin* devices, which currently dominates the tandem research, lack behind their *nip* counterparts in terms of efficiency and stability. Currently, researchers around the world are addressing these problematics in order to exploit the full potential of this class of materials and to achieve stable devices, as being mandatory for industrial production. Through the years, diverse approaches have been introduced with the purpose of increasing the PCEs of perovskite PV. For instance, several works focused on reducing the energy losses in the devices and consequently increasing the open-circuit voltages (V_{OC}) by using passivating agents[9,13,14], introducing interlayers[15,16] or by surface modifications.[17] Other approaches, instead, focused directly on improving the material quality through compositional engineering[18–20] or by the usage of additives.[21,22] Finally, work has been devoted to the optimization of the charge transport layers (CTLs) by minimizing transport losses or reducing the energetic offset between the layers.[23,24] On the other hand, various methodologies have been implemented aiming to improve the intrinsic stability of the material, as well as of the devices. For example, low-dimensional (2D) perovskites,[25–27] or a combination of high and low dimensional structures,[28,29] have been successfully implemented with the result of improved water and humidity resilience, while also hindering the out-diffusion of volatile organic cations, and finally leading to significantly improved long-term stability.[30] Other successful approaches allowed for better device stability by implementing self-assembled amphiphilic monolayers (SAMs)[31–33] or by sandwiching the perovskite between diffusion and water resistant layers[34–36], blocking the penetration of water and oxygen and the diffusion of the organic cation at the same time.

In this work, we introduce a poly(ionic-liquid) (PIL) as a multi-functional interlayer material to concomitantly increase the efficiency and the stability of different PSCs. Importantly, in the past, a large number of studies dealt with the implementation of ionic liquid (IL) salts in perovskite solar cells, introduced either as additives in the perovskite precursor solution to improve the material quality and stability[37–40] or as contact work-function modifier[23,41–43] to enhance charge collection. However, in most of the cases, the addition of the IL delivered only moderate efficiencies (with exception[40]). Also, when the IL is used as an additive to the perovskite solution, its effect on the final thin layer morphology and optoelectronic function is expected to be highly sensitive to the exact perovskite formulation and coating technique used.[44] This is distinctly different from our approach, where the PIL is coated onto the already existing perovskite layer. Polymer ionic liquids are “liquid”, i.e. their glass transition temperature is below room temperature, and as that, they are ion conductors which form a conformal coating on surfaces by spreading down even to nanometer dimensions. PILs have been used as polymeric solid electrolyte interface layer in electrochemical cells where it was shown that the

PIL not only improves the stability but also lowers the interface resistance.[45–47] PILs are also known to be extremely versatile due to the interchangeability of the counterion, allowing them to achieve high ionic conductivity, hydrophobicity, thermodynamic and thermal stability, as well as chemical durability.[47,48] However, despite a recent report where a type of room-temperature molten salt is used in the perovskite precursor,[49] to the best of our knowledge, PILs have not yet been demonstrated in MHPs cells as multifunctional and versatile interlayer.

Here, we employ an imidazolium-based PIL with a bis(trifluoromethane)sulfonimide (TFSI) counterion, abbreviated as [PeIm][TFSI], to modify the interface between a triple cation perovskite and a C_{60}-based electron transport layer (ETL). Density functional theory (DFT) calculations highlight that TFSI anion contained in the [PeIm][TFSI] couple can effectively stabilize under-coordinated Pb atoms at the surface, due to a favorable interaction between nitrogen and lead. In agreement with this prediction, neat perovskite layers coated with the PIL exhibit reduced non-radiative losses. More importantly, interfacial recombination at the perovskite-C60 interface is also strongly reduced. Detailed microscopic studies reveal a complex morphology of the PIL-covered perovskite, comprising polymer-containing insulting islands surrounded by TFSI rich areas. While the islands act as blocking layer between perovskite and C_{60}, preventing direct contact between the two materials the neighbouring well-passivated areas promotes the extraction of charges and provides a more ideal energy alignment between the layers. As a result, these solar cells exhibit outstanding V_{OC} and *FF* values of 1.17 V and 83% respectively, with the best devices reaching conversion efficiencies up to 21.4%. Additionally, the hydrophobic nature of the PIL counterions and the passivating behaviour of the PIL improves the stability of the device under maximum power point tracking and long-term shelf storage. Finally, we demonstrate the beneficial effect of the PIL in *nip* cells where the treatment modifies the interface between the perovskite and a Spiro-OMeTAD-based hole transport layer (HTL), increasing the *FF* and enhancing the reproducibility. The results from a large number of characterization methods, coupled with theoretical calculations, allows to rationalize the working mechanism of PIL in perovskite solar cells and to explore in details how this new class of interlayers effectively improve perovskite materials and devices, opening doors for the future applicability of this class of materials.

Results and Discussion

Device Performance

Our work focuses primarily on optimized *pin*-type devices,[50] in which the semiconducting polymer poly[bis(4-phenyl)(2,4,6- trimethylphenyl)amine] (PTAA) serves as the hole-transporting material in the device architecture: indium tin oxide, ITO (150 nm)/PTAA (8 nm)/ poly[(9,9-bis(30- ((N,N-dimethyl)-N-ethylammonium)-propyl)-2,7-fluorene)- alt-2,7-(9,9-dioctylfluorene)] dibromide (PFN-P2)/ perovskite (400–500 nm)/C_{60} (30 nm)/bathocuproine, BCP (8 nm)/Cu (100 nm).The perovskite absorber has the composition $(Cs_{0.05}(MA_{0.17}FA_{0.83})_{0.95})Pb(I_{0.83}Br_{0.17})_3$, with an optical bandgap of 1.62 eV. [51] The PIL is introduced between the perovskite and the C_{60} layer, as depicted in Fig. 1a) by spin coating a highly diluted solution (0.5 mg/ml in acetonitrile:isopropanol (1:4)) on top of the perovskite. The synthesis method and the characterization of the very same PIL used here is reported in a

previous study by Spanos et al.[46] Additional characterization of the PIL is reported in **Section 1, SI**. After that, the device is completed by depositing C_{60}, BCP and Cu by thermal evaporation, see Fig.1 a). The positive effect of the PIL treatment on power conversion efficiency is exemplified in the current-voltage (*J-V*) characteristics in **Fig. 1b**, where a parallel improvement of the V_{OC} and the *FF* is observed. Notably, the treated cells exhibit very minor significant hysteresis behaviour, **Fig. S2A (SI)**. The increase of the V_{OC}, reaching values up to 1.17 V, suggests that the presence of the PIL reduces the non-radiative recombination of charges at the interface between the perovskite and the C_{60}.[52] Moreover, the *FF* increases to outstanding values of nearly 83%, indicating that the PIL improves the charge extraction and reduces the transport resistance.[53] The average *FF* values averaged over a large number of devices plotted in **Fig. 1c** increases from below 77% for the reference cells to nearly 81% for the PIL containing ones. **Fig. 1c** also denotes a large improvement of the reproducibility of the device performance of the PIL-containing devices, which results also in a smaller spread of the *FF* and J_{SC} values. The combination of the improved V_{OC} and *FF* results in an efficiency enhancement from an averaged PCE of 19% for the reference cells to an average PCE of nearly 21%, again with a narrower distribution. The best device, **Fig. S2B (SI**) reaches a PCE of 21.4%, which approaches the best efficiencies reported for *pin*-type PSCs.[54,55] We note that the introduction of the PIL treatment does not affect the EQE_{PV} nor the absorption, **Fig. S3A-2B (SI)**, thus not influencing the bandgap of the perovskite absorber. To disproof that the improvement comes from just one of the two species of the PIL, in **Fig. S2C (SI),** we compare cells with imidazolium-based PILs using different counterions, namely [PeIm][Br] and [PeIm][PF_6]. Interestingly, [PeIm][Br] limits the performance of the device, whereas [PeIm][PF_6] gives identical results to the [PeIm][TFSI]. This finding suggests superior effects of fluoride containing hydrophobic anions over (hydrophilic) halides as counterions, consistent with earlier results[40], but may also imply that the improvement of the [PeIm][TFSI] does not come from only one of the two constituents. In line with this, devices implementing only a Li-TFSI modest increase in the device performance, see **Fig. S2D (SI)**, indicating the essentiality of having the TFSI ion embedded in a polymer matrix in order to efficienctly improve the solar cell device, as we will demonstrate below.

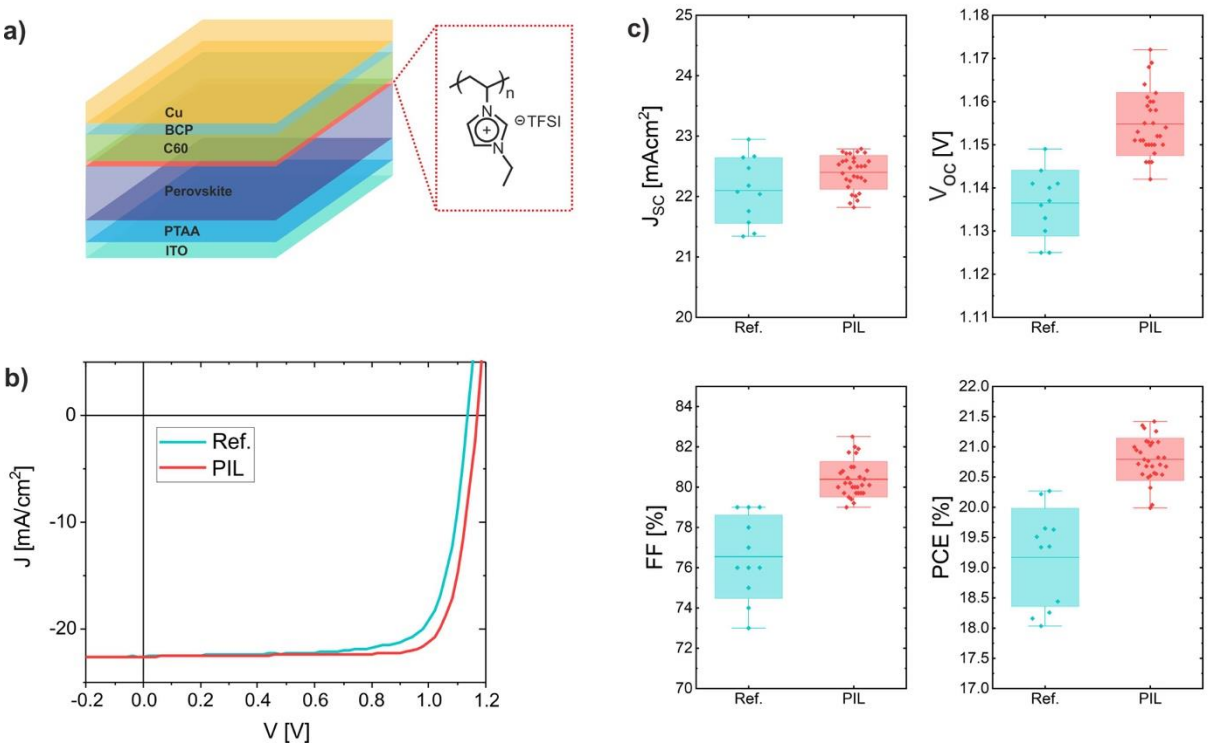

Figure 1*: a) Pin-type device layer structure with the chemical structure of the poly(ionic-liquid) (PIL), inserted between the perovskite and the C_{60}. b) Typical current-voltage characteristic for a reference untreated cell and for a PIL-modified cell in reverse scan at 0.025 V/s (hysteresis shown in Fig. S1A SI). c) Device parameter statistics for the reference cells and the PIL containing cells; the boxes indicate the standard deviation.*

DFT Calculations on the PIL-Perovskite Interaction and Defect Passivation

To understand in detail the interaction at the perovskite surface in the presence of [PeIm][TFSI] couple, density functional theory (DFT) calculations are carried out by using the PBE functional[56] and including dispersion interactions. The details of the DTF simulation can be found in **SI Section 4**. The results highlight that TFSI anion contained in the [PeIm][TFSI] couple can effectively stabilize under-coordinated Pb atoms at the surface, due to a favourable interaction between nitrogen and lead. However, since the direct substitution of MAI molecules with PIL at the perovskite surface is energetically disfavored, [PeIm][TFSI] mainly acts as a passivating agent in regions deficient of MAI. The favorable adsorption of TFSI in these MAI-poor regions results in an upshift of the valence band maximum (VBM) and a decrease in work function (WF). The passivation effects are investigated further by looking at iodine Frenkel (interstitial/vacancy pair) defect formation energy (DFE) before and after [PeIm][TFSI] passivation. Interstitial iodine has been shown to be a major source of the increased non-radiative recombination at the surface and in the material bulk.[57] Our DFT calculations show that the iodine Frenkel DFE is largely increased by the presence of the [PeIm][TFSI] couple at the surface, making the formation of this type of defects disfavoured by ~0.8 eV with respect to the un-passivated PbI_2-terminated surface when the surface is half passivated by [PeIm][TFSI] (0.55 eV with respect to the half MAI-terminated surface). Importantly, these theoretical results are also confirmed by refining the level of theory by performing hybrid PBE0

functional[58] single point calculations at the PBE relaxed geometries. The passivation effects are ascribed mainly to the steric interaction between the PIL layer and the iodine interstitial at the surface. As shown in Figure 2e-f, the formation of iodine interstitial defect in the Frenkel couple leads to a weakening of the Pb-N bond in the TFSI-passivated surface (Pb-N bond lengths > 4 Å) with an overall destabilization of the surface. As a consequence, in this case, the DFE for this type of defects is increased. However, despite the effective passivation effect of the perovskite surface, in a complete solar cell device, the detrimental interface recombination across the layers must also be reduced. Hence, we will show how having also an insulating polymer matrix in contact with the transport layer is essential to increase the device performance.

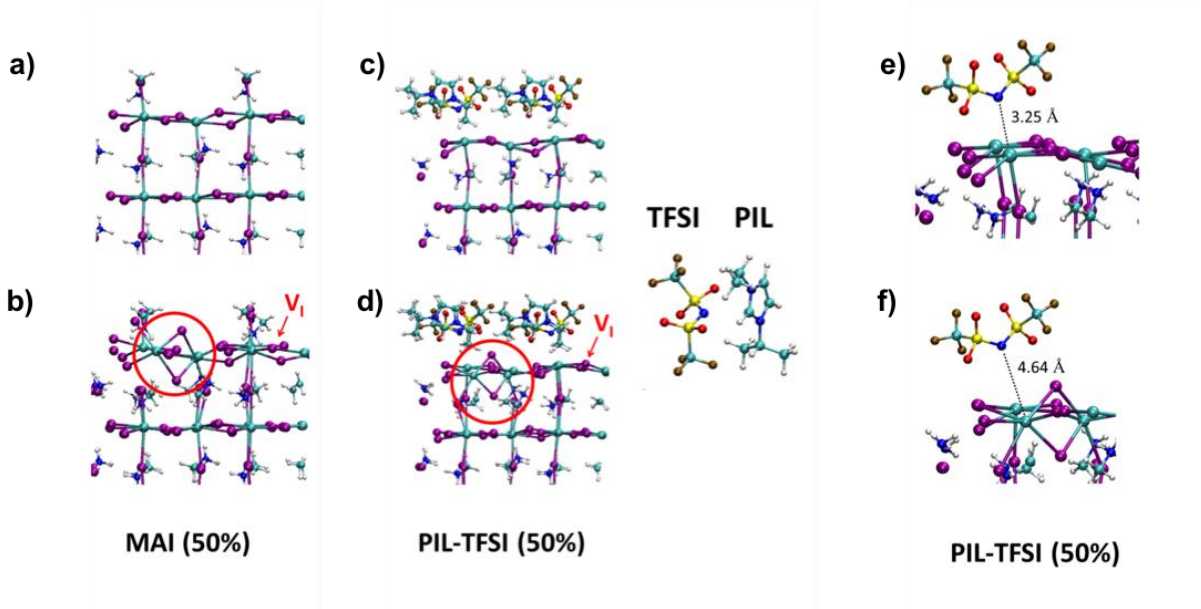

Figure 2*: a)-b) Structure of MAI-half terminated perovskite surface with and without Frenkel defect, respectively. c)-d) Structure of PIL-half terminated perovskite surface with and without Frenkel defect, respectively. In e) and f) the structural details of the TFSI anion absorbed on the perovskite surface, with and without Frenkel defect, are given.*

Morphology and Chemical Composition of the PIL-Covered Surface

In **Fig. S5 (SI)**, X-ray diffraction (XRD) measurements indicate that the PIL surface treatment does not influence the crystal structure of the perovskite, nor additional phases were detected. However, contact angle measurements revealed that the PIL treatment increases the hydrophobicity of the surface, **Fig. S6 (SI)**, as expected from the hydrophobic character of [PeIm][TFSI].[45] The top surface scanning electron microscopy (SEM) images in **Fig. S7A (SI)**, however, show that the surface coverage is not homogeneous. Instead, the PIL forms island-like features on top of the typical cobblestone perovskite surface. Energy-dispersive X-ray (EDX) elemental-distribution maps acquired on the surface of the PIL treated sample **(Fig. 3b-c**) confirm that these islands are composed of a carbon-rich material, presumably mostly the polymer [PeIm]. On the other hand, the O signal, not detectable in the reference sample, is attributed to the TFSI counter-ion (a more detailed discussion can be found in **Section 8**, **SI**). As detailed in **Fig. S8A (SI)**, the O and C on the top surface are anticorrelated, meaning that

the surface features areas rich in the positively-charged polymer, surrounded by regions covered predominately by the TFSI anion. This anticorrelation may be due to the fact that the PIL will not attach to MA- or I-terminated surfaces but rather to regions deficient of MAI, as suggested by the DFT calculations described earlier. Unfortunately, our techniques do not allow to correlate the initial surface composition to the chemical distribution of the PIL after spincoating. Additionally, EDX maps and line-scans of the cross-section of the PIL-treated sample in **Fig. 3g** exhibit higher concentrations of C and O on the surface of the film, indicating that both, the polymer and the counter-ion, do not diffuse in the perovskite bulk to an appreciable extent.

Surface Passivation

To investigate the proposed passivation of defects at the perovskite surface by the PIL, cathodoluminescence (CL) images were recorded and correlated with the surface morphology (**Fig. 3d-f)**. This comparison reveals a dominant enhancement of the CL in the areas around the polymer islands enriched by the TFSI counterion (**Fig. 3e**), confirming the DFT results. In fact, in full agreement with the TFSI passivation effects revealed by our calculations, N can act as Lewis base and passivate I vacancies, uncoordinated Pb^{2+}, or metallic Pb clusters, stabilizing the surface and effectively reducing the trap density.[59–62]
The CL of the perovskite underneath the polymer islands is also enhanced though to a smaller extent. (**Fig. 3f** and **Fig. S8B, SI**). It has been proposed that uncoordinated I, antisite PbI_3 as well as MA^+ or FA^+ vacancies can be potentially passivated by the imidazolium group.[40,59,63] Interestingly, in **Fig. 3e** the TFSI-rich surface features small spots of increased luminescence, which are not present in CL maps of the neat perovskite. This suggests that trap passivation is indeed more efficient at specific locations, which are uncorrelated with the morphology, as visible when the SEM and CL images are superimposed, **Fig. S8C (SI)**. Generally, this scenario indicates that both species contained in the [PeIm][TFSI] can effectively passivate surface defects preventing the non-radiative recombination of charges.

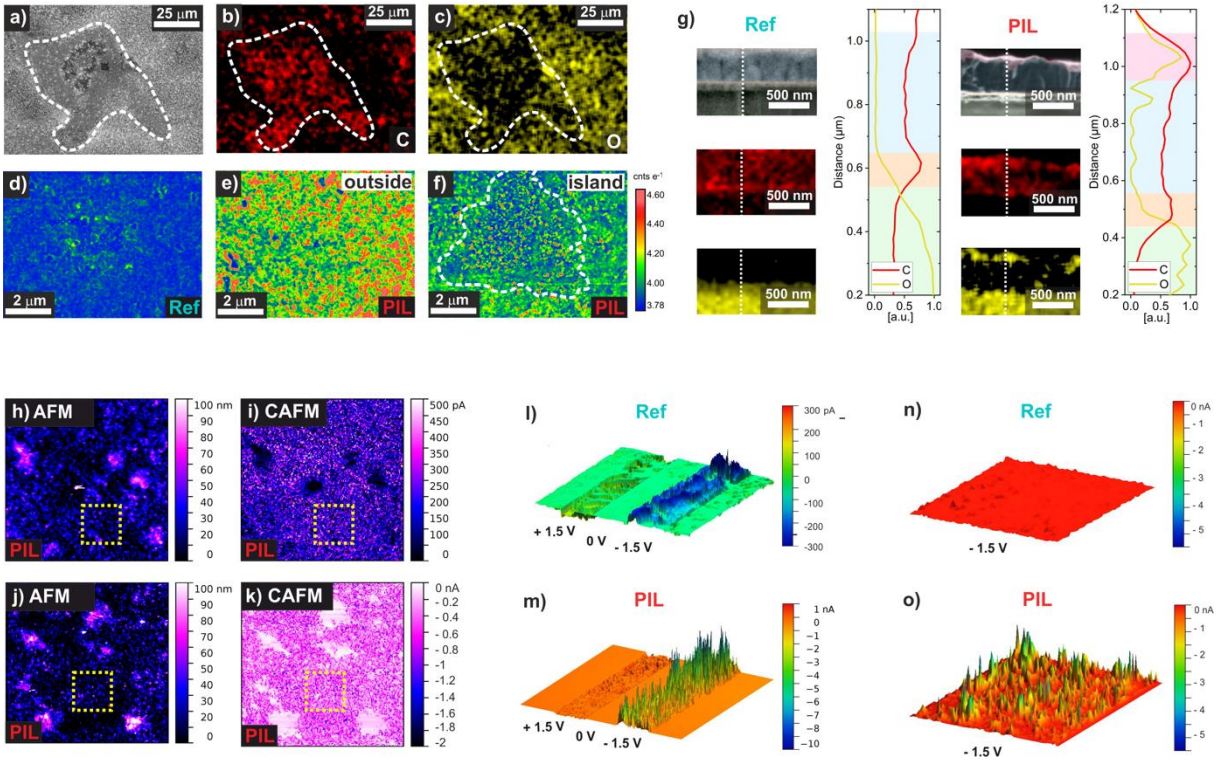

Figure 3*: a) SEM image showing a typical polymer-rich island on the surface of the perovskite (dashed contours). Corresponding EDX elemental-distribution maps for b) carbon and c) oxygen showing the enhancement and depletion of the signal on the island region, respectively. CL map of d) untreated perovskite film, e) PIL-treated film outside the polymer island and f) PIL-treated film with a polymer island. Notably, in f), luminescent spots are visible from the emitting perovskite beneath the non-emitting polymer island. g) SEM and EDX cross-section images for reference and PIL treated perovskite films with corresponding EDX line scans. For both samples, the C signal appears to be enhanced on the ITO/PTAA/perovskite interface, due to the PTAA. The O signal is concentrated on the glass region in both samples while the PIL-treated sample shows in addition the O signal at the surface indicating the presence of the TFSI molecules in that region. AFM topography images (40x40 µm^2) of reference and PIL-treated perovskite h) and j) show the presence of the polymer island, with heights between 50-100 nm. The corresponding CAFM images i) and k) reveal that the polymeric island presents a strong insulating character, reducing drastically the current signal when both a positive i) and a negative k) bias is applied. The dotted yellow lines indicate exemplary areas scanned in l)-o). l) 3D CAFM images (3x3 µm^2) of the untreated perovskite layer. The image represents a scan while applying different voltages from -1.5 V to 1.5 V in step-like fashion. m) 3D CAFM images (9x9 µm^2) of a perovskite layer treated with PIL. The image represents a scan with the same conditions of l). n) and o) shows 3D representations of two areas of 3x3 µm^2 with the same current scale to directly compare the reference perovskite and the PIL treated film upon applying a bias of -1.5V.*

In light of the presents of large and thick polymer-containing islands, the improved *FF* of the PIL-containing device comes as a surprise. Atomic force microscopy (AFM) and conductive AFM (CAFM) analyses provide microscopic information on the correlation between surface topography and charge injection/extraction properties (instrument configuration is depicted in **Fig. S9A SI**). From large area surface scans, we observe that the reference sample exhibits a rather smooth topography and low uniform conductivity (**Fig. S9B, SI**). In contrast, the thick polymeric islands in the PIL treated surface, with a height of roughly 100 nm (**Fig. S9C, SI**),

are highly insulting at both polarities, as presented in **Fig. 3h-k**. Interestingly, the areas outside the islands show enhanced conductivity compared to the reference perovskite. To investigate this finding further, in **Fig. 3l-o** we performed CAFM measurements on these areas with higher spatial resolution, as indicated by the yellow lines in **Fig. 3h-k**. Here, the voltage (applied to the tip) is swept from positive to negative bias during the vertical scan in a step-like fashion. Surprisingly, while the reference samples exhibit low current signal (pA range), which is symmetric for positive and negative bias, the PIL treated surface demonstrates a tremendously increased current, approaching values of ~10 nA. The current enhancement is larger when the tip is biased negatively, namely electron injection from the tip into the conduction band of the PIL-covered perovskite sample is more efficient than hole injection into the valence band. The result is in accordance to the largely improved *FF* of the PIL-treated *pin*-type devices, where electrons enter or exit the perovskite through the top surface, similarly as found by Xu *et al.* for a similar set of experiments.[64] Interestingly, when CAFM images of the two samples are directly compared on an area of $3x3\ \mu m^2$ in the same current range, **Fig. 3n-o**, it is evident that the PIL treated surface features inhomogeneously distributed highly conductive points, which create isolated spikes in the current signal, reminiscent of the CL luminescence pattern. Also in this case, these spikes do not correlate with the surface topography. Though our methods do not allow us to correlate the positions of spikes of high conductivity and CL, it is not unlikely that both have the same origin, related to surface modification on an atomic level. As suggested by the DFT calculations, the application of the PIL causes a drastic increase of the DFE for specific defects at the surface. As a result, trapping of photogenerated (and dark-injected) carrier would become less likely, with the benefit of improved charge extraction (injection) and reduced trap-assisted recombination. We note here that the spikes in C-AFM only appear in the regions outside the polymer islands which indeed suggests that they are related to the passivation of local traps by the TFSI, as emerged from DFT calculations. Related to this interpretation, we observe that the PIL treated perovskite shows a 3-fold improvement in lateral conductivity and lower contact resistance compared to the reference perovskite **Fig. S10 (SI)**, indicating that charge carrier trapping is less likely. Interstingly, while the treatment with the PIL increases the surface conductivity and concomminently improvs the FF, dark *J-V* characteristics in **Fig. S11 (SI)** reveal lower leakage currents in the low voltage region for the PIL treated devices. Such leakage currents are usually attributed to pin-holes or a very heterogeneous layer morphology. The PIL may fill such imperfections with the result of a higher shunt resistance potentially increasing the *FF*.

XPS/UPS studies of the PIL-Covered Perovskite Surface

The above results show that the PIL passivates defects at the perovskite surface and that this effect is most prominent in the TSFI rich areas not covered by the thick polymer islands. On the other hand, our DFT calculations ascribe the passivation mainly to the steric interaction between the PIL layer and the iodine interstitial at the surface and not to the formation of new chemical bonds. To confirm this interpretation, X-ray photoelectron spectroscopy (XPS) and UV-photoelectron spectroscopy (UPS) was employed. The X-ray photoemission spectroscopy (XPS) survey spectrum of the PIL treated perovskite presents all the expected core level peaks of the characteristic elements present in both the neat perovskite and the neat PIL (**Fig. S12A,**

SI). This confirms that in the areas surrounding the polymer islands, the PIL is thin enough to permit photoelectrons from the perovskite surface to escape. High-resolution XPS measurements, presented in **Fig. 4a**, show that the deposition of the PIL on top of the perovskite surface induces a shift in all core levels of the perovskite elements towards lower binding energies by about 0.2 eV compared to the reference sample. Importantly, the absence of any preferential shift of the XPS core levels rules out that strong chemical bonds form between the PIL and specific atoms at the perovskite surface, meaning that the interaction between the two components is of electrostatic nature. This is also in line with the DFT calculation results, where the TFSI-Pb interaction gets weakened when the PIL coverage is increased, **Table S4**. Therefore, in our experiments, most probably the large coverage of perovskite surface with PIL, even if ultra-thin, is prone to a weaker TFSI-Pb interaction, otherwise visible as preferential shift of the Pb binding energies. Moreover, since the DFT calculation also pointed out that the TFSI-Pb interaction is possible exclusively in regions where MA is absent, the preferential shift can be less visible in the XPS spectra.

The UPS spectra in **Fig. 4b** confirm a ca. 0.2 eV shift of the valence band maximum (VBM) closer to the Fermi level for the PIL treated perovskite, in agreement with the predicted upshift of the VBM from DFT calculations. Surprisingly, the upwards shift in the VBM towards the Fermi level does not translate into a corresponding increase of the work function (WF). Such a scenario is only possible if the PIL additionally creates a surface dipole pointing towards the vacuum. Also in line with the CL results, this picture indicates a preferential layering of the PIL molecule with the TFSI in direct contact with the perovskite surface and the imidazolium group on the outside, as indicated in **Fig. 4c**. This phenomenon is associated to the nature of the polyionic liquids, where the arrangement of the two ions induces a Maxwell-Wagner-Sillars type interfacial polarization.[65,66]

To understand the impact of the PIL on the energetic alignment with respect to the C_{60} ETL, UPS measurements were performed on samples with 20 nm of C_{60} deposited on top, **Fig. 4d**. The resulting interfacial energy diagram is depicted in **Fig. 4c**. It is evident that the PIL-treated perovskite film exhibits a better alignment of the perovskite conduction band edge with the lowest unoccupied molecular orbital (LUMO) of the C_{60} layer, promoting charge extraction by eliminating the small extraction barrier found for the reference sample. Additionally, the surface dipole introduces a downwards shift of the highest occupied molecular orbital (HOMO) of the C_{60} with respect to the VBM of the PIL-treated perovskite, improving the contact selectivity. Overall, we observe that the application of the PIL besides passivating the surface traps also provides a better energy allignment, possibly due to the formation of a surface dipole, beneficial in terms of increased *FF* due to better charge extraction.

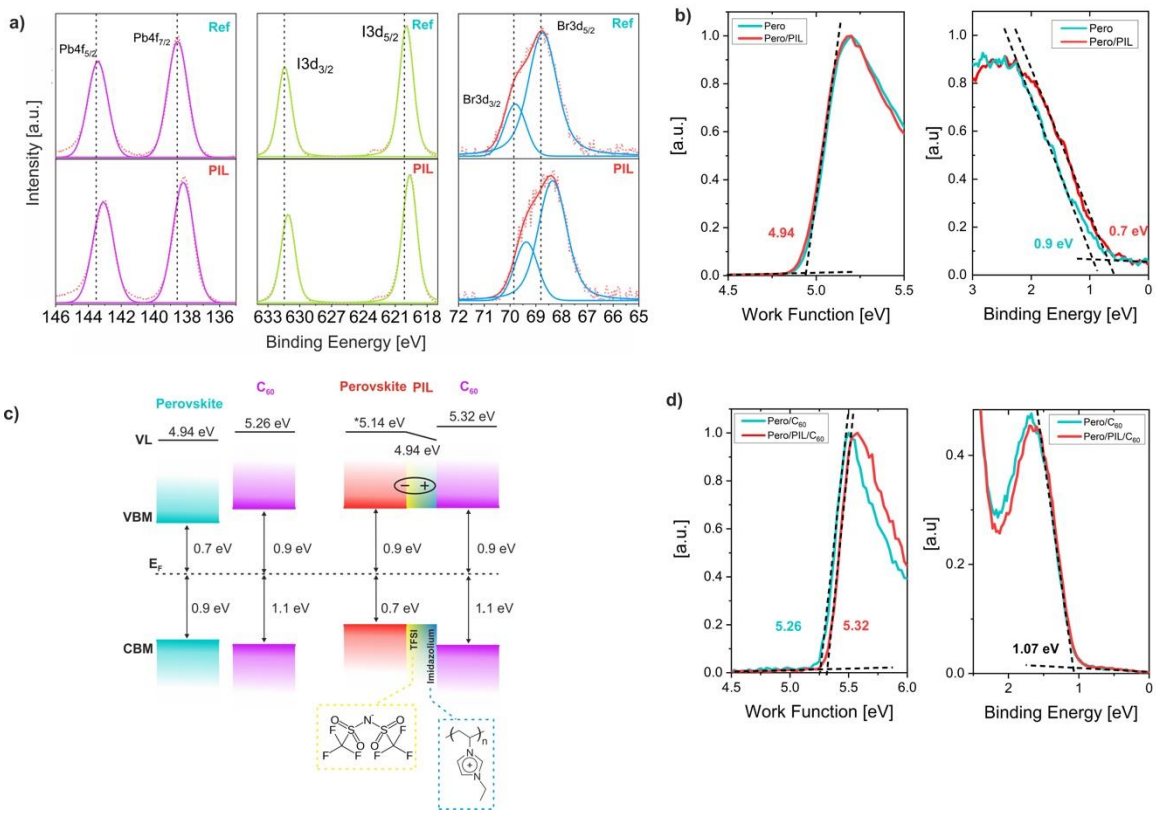

Figure 4: *a) High resolution XPS spectra of perovskite films with and without PIL treatment for characteristic perovskite elements to highlight the core level shifts. b) Ultraviolet photoelectron spectroscopy (UPS) results for work function and valence bands (probed by X-ray) of the reference and PIL treated neat perovskite and c) with C_{60} films on top of the perovskite layer with and w/ PIL treatment. c) Interfacial energy levels of the perovskites/C_{60} interfaces as obtained from the photoemission spectroscopy data shown in panel (b) and (d). Note, all perovskite films were deposited on top of ITO/PTAA substrates and UPS as employed here probes only the surface energetics of the studied sample*

Photoluminescence, quasi-Fermi level splitting and V_{OC}

It has been shown that free carrier recombination in perovskite solar cells is largely limited interfacial recombination at the interface between the perovskite absorber and the CTL.[67–69] The results summarized above suggest that this interfacial recombination is reduced by the PIL in two ways. First, the passivation of the perovskite surface by the PIL will reduces the density of traps available for interfacial charge recombination. In addition, the presence of large polymer island limits the interface area between the perovskite and C_{60}. An elegant way to investigate surface and interface recombination is transient and steady state photoluminescence.[70] This is because the photoluminescence intensity is a direct measure of the carrier density in the perovskite and with that of the quasi-Fermi level splitting (*QFLS*). As shown in **Fig. 5a-b,** the comparison of the steady state photoluminescence of the neat films and the complete cells reveals a significant reduction of non-radiative recombination in the PIL-treated samples. We find that the photoluminescence quantum yield (*PLQY*) of the bare material increases from 1.2% for the reference sample to 7.2% for the PIL treated one, consistently with the decreased trap density due to the increase in Frenkel defect formation energy observed in

DFT simulations. Following the approach presented in **Section S13 (SI**) and in previous works,[71,72] by combining the information from *PLQY* measurements and the *EQE* spectra allows to calculate the quasi-Fermi level splitting (*QFLS*) in the absorber, and relate this to the thermodynamic radiative limit for these cells. The latter is found to be ~1.32 eV for both samples. The *QFLS* in the neat material essentially corresponds to the maximum achievable V_{OC} for a given perovskite and illumination condition. We find that the *QFLS* increases from ~1.20 eV to ~1.26 eV for the PIL-treated perovskite, indicating that the non-radiative losses in the neat material are reduced from 120 meV to 60 meV. This substantial reduction in non-radiative recombination is qualitatively consistent with the increase in CL emission, where the passivation of the PIL is visualized on the surface. Moreover, in full devices, the *PLQY* of the treated sample increases from 0.1% to nearly 0.5%, increasing the *QFLS* from 1.14 eV to 1.18 eV, in good agreement with the measured V_{OC} of the cells (1.14 V and 1.17 V, respectively). This also highlight how, besides the beneficial passivation effects of the TFSI passivation, in the full device, the polymer insulating matrix helps to reduce the overall recombination across the interface with C_{60}. Consequently, the total non-radiative losses in the complete device are reduced from 180 meV to 140 meV. Consistently, the electroluminescence efficiency (EQE_{EL}) presented in **Fig. S13 (SI)** exhibits a more than a two-fold increase for the PIL treated device. These results highlight the beneficial effects of the newly-formed perovskite/PIL/C_{60} junction, where interfacial non-radiative recombination is reduced, allowing for higher *QFLS* and V_{OC}. In agreement with this picture, the photoluminescence decays (TRPL) in **Fig. 5c** show that the neat perovskite and the perovskite covered with C_{60} exhibit longer decays when they are treated with PIL. By fitting the decay with a double exponential model and extracting the lifetime from the slower component characteristic for SRH recombination,[52] upon PIL treatment the lifetimes increase from 400 ns to 900 ns for the neat material and from 60 ns to 110 ns for perovskite/C_{60} junction. This again confirms the effectiveness of the combine effects of the TFSI ion passivation and the insulating polymer matrix

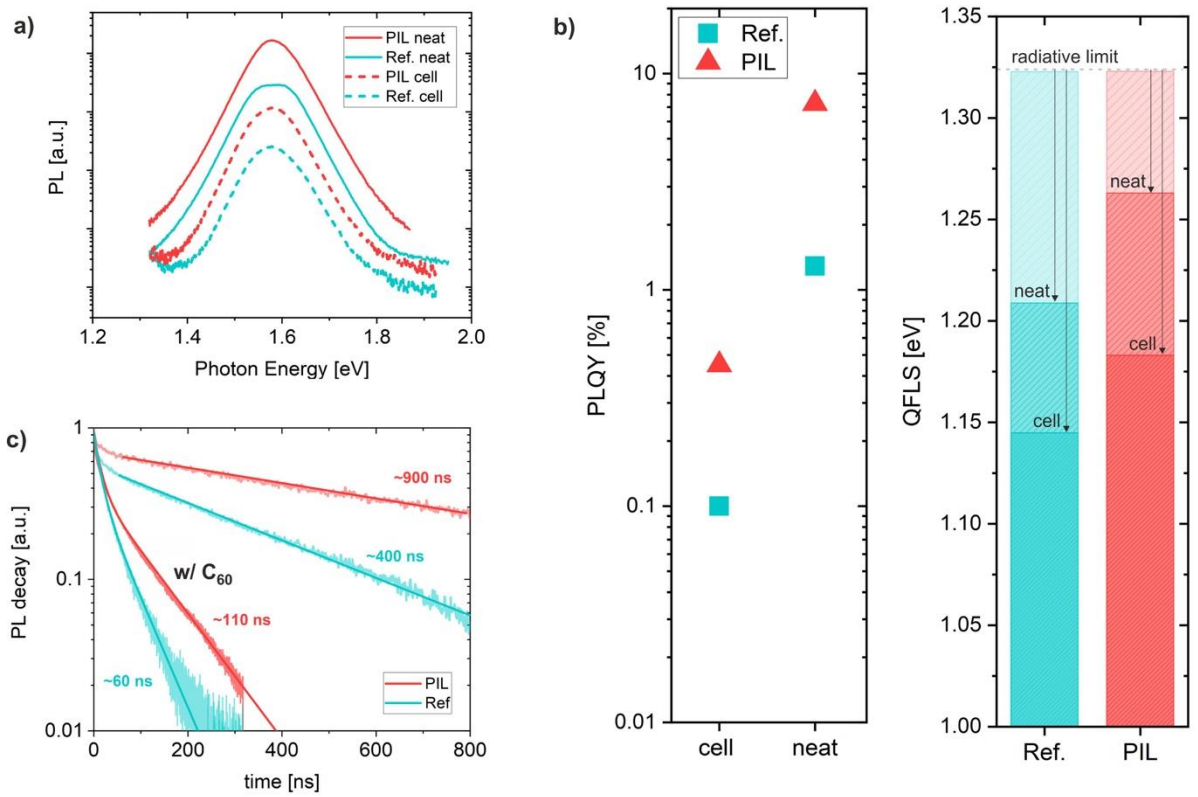

Figure 5*: a) Photoluminescence spectra of the neat perovskite and complete cells for the reference and the PIL-treated samples. b) Photoluminescence quantum yield measured on the neat material and the complete device stack with the respective calculated quasi-Fermi level splitting. The calculated radiative limit is shown to highlight the energy losses with respect to the theoretical thermodynamic limit. c) Normalized TRPL decays of the reference and the PIL-treated perovskite, with and without C_{60} deposited on top. In both cases the PIL-treated samples show longer lifetimes denoting an effective reduction of non-radiative recombination.*

Device Stability

Remarkably, introducing the PIL in the device stack does not only improve of the material quality and the device performance, but also the stability of the devices. We find that non-encapsulated device comprising the PIL exhibit significantly increased stability under maximum power point (MPP) tracking in inert atmosphere as compared with the reference cell. Notably, the PIL treated cell retains 90% of its initial efficiency after more than 90 h at 50° C, as presented in **Fig. S15 (SI)**. We additionally measured long (700h) MPP tracking, for PIL-treated and reference samples utilizing SnO_2 instead of BCP, to replicate and test the PIL on the common configuration used in tandem devices. This allows to remove the contribution in degradation of the BCP itself and reveal more accurate information on the degradation of the perovskite material. The MPP results averaged over multiple cells, presented in **Fig. 6c**, show that the PIL device significantly outperformed the reference cell retaining its efficiency at 80% of the initial value after 700h, otherwise reached after 120h for the reference device. Importantly, we found that, despite in the FF and J_{SC} the difference in degradation is not dramatic (**Fig. S16, SI**), the V_{OC} values revealed that the reference samples undergo severe V_{OC}

losses after ~120h, otherwise almost absent in the PIL sample, indicating superiority of the top interface in this type of devices. Interestingly, when comparing the MPP results of samples with BCP and SnO_2, in the reference device, the protecting effect of SnO_2 is clearly visible with enhanced stability. On the other hand, the stability of PIL sample does not further increase significantly when the SnO_2 is present. This finding confirms that the PIL layer alone can already provide the protecting effects at the perovskite surface, similarly as provided by the compact SnO_2. Moreover, PIL treated non-encapsulated devices stored under inert atmosphere and exposed to indoor light can fully retain their PCE of ~21% during 10 months of shelf storage, as exemplarily shown in **Fig. 6 a)** and **b)**. A larger set of devices aged for up to 15 months is presented in **Fig. 6 d),** demonstrating that the PIL-treated devices exhibit a longer shelf life compared to the reference devices, which degrade significantly over time. The improved stability may originate from two main factors. On one hand, the new hydrophobic surface induced by the PIL treatment potentially helps to prevent the penetration of water and moisture, which leads to degradation of the perovskite material, following the mechanism proposed in previous studies.[30,73] On the other hand, the PIL layer improves the stability of the perovskite from a structural point of view. As proposed in previous studies, the presence of surface defects and trapped charges can accelerate moisture, oxygen- and light-induced degradation.[74,75] Additionally, in presence of surface defects, light exposure can trigger the migration of iodine species from bulk to the surface leading to an intrinsic degradation of perovskite material.[49] Given the large increase in Frenkel defect formation energy observed in induced by the PIL layer, the surface defect density is largely reduced and these effects are mitigated, leading to increased intrinsic stability as previously observed.[77,78]

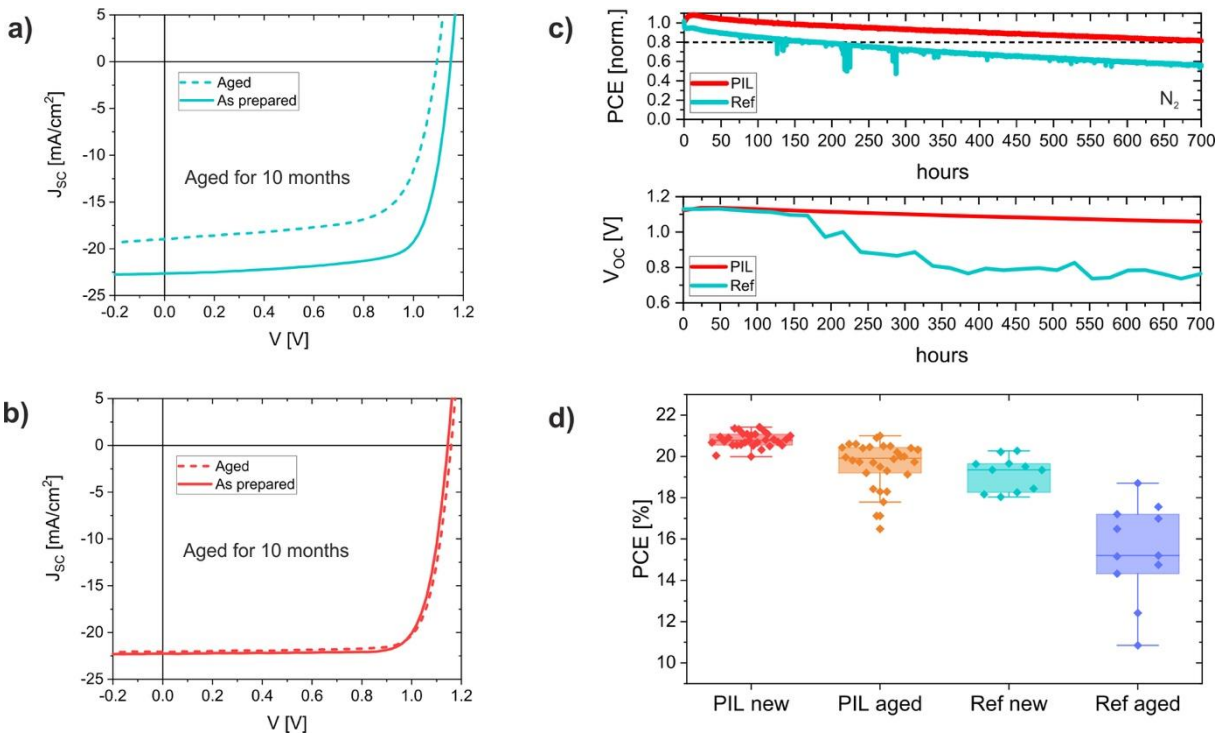

Figure 6*: a) and b) JV scans of as-prepared and 10 months aged reference and PIL treated devices. The samples were stored under N_2 atmosphere, non-encapsulated and exposed to indoor room light conditions. c) Averaged Maximum Power Point (MPP) tracking for 3-6 devices at 1 sun illumination conditions under N_2 atmosphere at 25°C for non-encapsulated cells with and without PIL, utilizing SnO_2*

instead of BCP. While the PCE of the reference device drops below 80% after roughly 120 h, the PIL device retains 80% of its efficiency even after 700h at MPP. The V_{OC} of the best cell under constant illumination is also reported showing severe degradation for the reference samples, otherwise almost absent in the PIL cell. d) Statistics of the PCE of the as-prepared (new) and aged (old) pin devices with and without PIL treatment. The aging time varies from 6 to 15 months, during which the samples were stored in nitrogen under room light.

Model and Generality for the Role of the PIL in Improving Device Performance

From the combination of all these measurements and DFT calculations, we propose that the PIL forms a multi-functional interlayer, as schematically represented in **Fig. 7**. First, the passivation of traps causes an overall improved carrier extraction/injection and reduced trap-assisted surface recombination, seen as a significant improvement of both the FF and the V_{OC}. Second, the polymer component in the PIL forms insulating islands, spatially separating the holes in the perovskite from the electrons on C_{60} and decreasing the possibility for non-radiative recombination of charges across this interface. It is well established that decreasing the interfacial area of the active absorber to the charge extraction contact is a powerful approach to reduce non-radiative interfacial/surface recombination.[15,79] In addition, the PIL may fill pinholes and voids, being the reason for reduced leakage and a higher reproducibility of the device performance. The role of the polymer component improving the device performance becomes evident when comparing with the changes introduced upon treatment with Li-TFSI (which does not contain the polymeric cation), *see* **Fig. S2D (SI)**. As expected, Li-TFSI mildly increases the device performance to a smaller extent than upon inclusion of the PIL, highlighting the importance of having the passivation action of the TFSI ion in combination with the insulating polymer matrix in order to fully improve the efficiency of the resulting device.

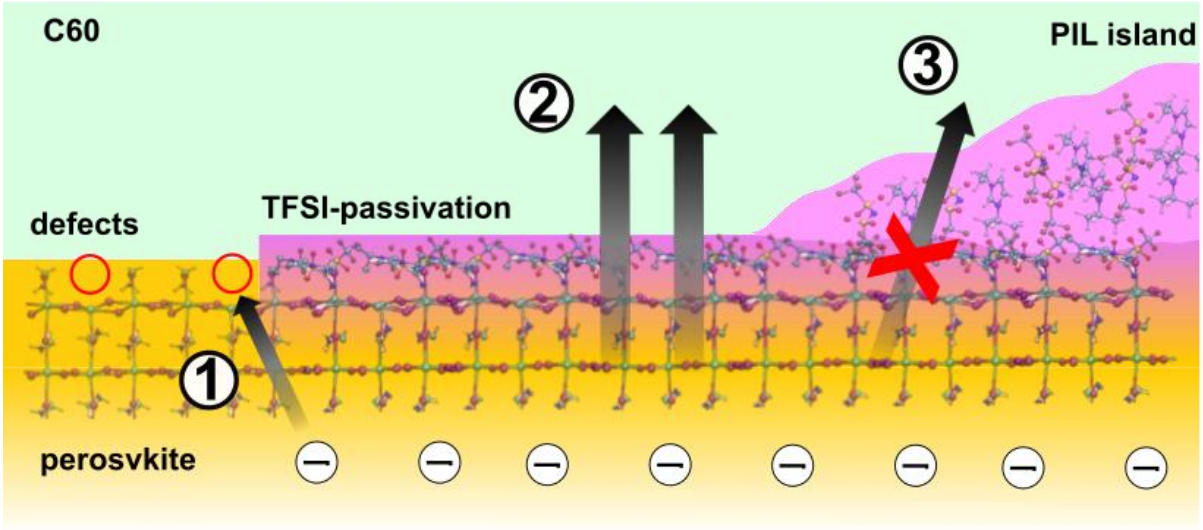

Fig. 7: *Schematic representation of the perovskite / ETL interface in the presence of PIL based on our experimental and theoretical results. 1) Possible non-radiative recombination pathway at the perovskite surface due to trapping at MA vacancies. 2) TFSI-passivate regions with reduced trap density and enhanced charge extraction. Here electrons do not undergo non-radiative recombination due to defects*

and can be effectively extracted. 3) The thick insulating polymer island effectively reduce the interface area physically spacing the perovskite and C60. As such, the interface recombination happening across this layer is reduced.

Finally, as a proof of concept, to corroborate the generality of this surface treatment, we expand our study to planar and mesoporous *nip* devices utilizing a 1.6 eV bandgap perovskite (**Fig. S17, SI**). As in the *pin*-type cells, the PIL is deposited on top of the perovskite surface, but for this device structure being in contact with the Spiro-OMeTAD-based HTL. Also in this case, the introduction of the PIL at the perovskite/HTL interface results in an increased *FF* and V_{OC}. As for *pin* cells, the PIL treatment results in a more ideal contact with the transport layer attached in both configurations. However, the improvements are particularly visible in mesoporous TiO_2 devices. Interestingly, the reduction of interface recombination is less visible in *nip* devices compared to *pin* cells. This is possibly due to the significant non-radiative recombination still occurring at the perovskite/ETL interface, as reported recently.[72] Nevertheless, independently on the specific architecture, the final PCE of the nip cells is improved upon PIL addition. We do not exclude that additional [PeIm][TFSI] in contact with Spiro-OMeTAD could also induce additional unintentional doping at the HTL.[80] In **Fig. S18, SI**, the study is extended to different perovskite systems, namely double cation narrow bandgap (1.54 eV)[81] and MA-free large bandgap (1.80 eV). Also in this case, the PIL samples demonstrated their superiority respect to the reference ones in terms of V_{OC} in the case of the low bandgap and FF in the case of large bandgap system. These results suggest how in the low energy gap cell the PIL at surface effectively reduces the detrimental recombination at the ETL interface, while in the large energy gap cell it might provide a better alignment between the layers enhancing the charge extraction.

In conclusion, we implemented a novel multi-functional interlayer based on imidazolium-based poly-ionic liquid [PeIm][TFSI]. By combining a large variety of experimental techniques with theoretical calculations, we were able to provide detailed machanistic insights on the PIL-perovskite system. Our results shed light on the specific interactions between the [PeIm][TFSI] couple and the perovskite surface, providing general understanding on the possible passivation routes. As such, we prorpose how the combination of an effective surface passivation specie, as TFSI, embedded in a insulating polymer matrix, is able to reduce non-radiaitve recombination, in the perovskite and across the interfaces, enhance the charge extraction and prolong the stabiliyt, all at once. Hence, contrary to clssic interlayers and simpler ILs, this optimization rute provide an efficient methods to concomitantly increase the V_{OC}, *FF* and stability of PSCs. Moreover, this approeach proved to be applicable to different cell architectures, perovskite compositions and perovskite bandgaps. Given the generality of this multifunctional layer, we expect a broad application of PILs in the field of perovskite research, including also inorganic perovskites and tandem solar cells.

Acknowledgements:
S.A. acknowledges funding from the German Federal Ministry of Education and Research (BMBF), within the project "Materialforschung für die Energiewende" (grant no. 03SF0540), and the German Federal Ministry for Economic Affairs and Energy (BMWi) through the "PersiST" project (grant no. 0324037C). Additional funding came from HyPerCells (a Joint Graduate School of the Potsdam University and the HZB), the Deutsche Forschungsgemeinschaft (DFG, German Research Foundation) – Project-ID 182087777 – SFB 951) and the BMWi through the "P3T grant (grant no. 03EE1017C). G.G. acknowledges the "HY-NANO" project that has received funding from the European Research Council (ERC) Starting Grant 2018 under the European Union's Horizon 2020 research and innovation programme (Grant agreement No. 802862).

Author Contributions:
P. C. performed all the *pin* cell fabrication, photoluminescence studies, SEM, stability measurement and wrote the manuscript; D.S.C synthesized all the PILs and performed XRD and contact angle measurement; S.C.D. performed the EDX and CL measurements and analysis; F.Z. performed XPS and UPS measurements; A.A.S. and L.K. fabricated the *nip* devices; B.L and F.P.C. helped during the fabrication of cells for stability measurements; L.P.T. performed the conductivity measurements; H.K. performed the long term stability measurements; C.M.W. helped during the stability measurements and assembled the experimental setup; B.S. performed the AFM and C-AFM measurements; E.G.P. fabricated the low bandgap devices, I.L. performed and analyzed XPS measurements; A.A. supervised the long term stability measurements; N.K. supervised the XPS and UPS measurements and helped during the interpretation of the results; B.R. supervised the fabrication of *nip* cell at HZB and helped during the interpretation of the results; D.M., L.G. and F.D.A. performed and interpreted the DFT simulations; G.C. supervised the *nip* cell fabrication at EPFL and helped during the interpretation of the results; D.A. supervised the EDX and CL analysis and helped during the interpretation of the results; M.K.N. supervised the *nip* cell fabrication at EPFL and helped during the interpretation of the results; M.S. helped during photoluminescence measurements, the interpretation of the results and contributed in writing the manuscript; S.A., M.A and D.N. supervised the work, helped during the interpretation of the results and contributed in writing the manuscript.

Competing Interests
The authors declare no competing interests.

Data availability
The data that support the plots within this paper and other findings of this study are available from the corresponding authors upon reasonable request.

Experimental Methods

***pin* Device Preparation:** Patterned indium-doped tin oxide (ITO, Lumtec, 15 ohm sqr.$^{-1}$) was washed with acetone, Hellmanex III, DI-water and isopropanol. After microwave plasma treatment (3 min at 200 W) poly[bis(4-phenyl)(2,4,6-trimethylphenyl)amine] (PTAA, Sigma-

Aldrich, Mn = 7000–10000, PDI = 2–2.2) in a concentration of 1,5 mg/ml was spin-coated at 6000 rpm for 30 seconds and immediately annealed for 10 minutes at 100º C. The PTAA was additionally treated by dynamically spin coating a diluted solution (0.5mg/mL in Methanol) of poly[(9,9-bis(30- ((N,N-dimethyl)-N-ethylammonium)-propyl)-2,7-fluorene)- alt-2,7-(9,9-dioctylfluorene)] dibromide (PFN-P2). The perovskite layer was formed by spin coating a DMF:DMSO solution (4 :1 volume) at 4500 rpm for 35 seconds. After 10 seconds of spin coating, 300 mL of |Ethylacetate (antisolvent) was dripped on top of the spinning substrate. The perovskite is annealed for 2 minutes at 100º . The PIL is then spincoated on the perovskite, by spin coating a highly diluted solution (0.5 mg/ml in acetonitrile:isopropanol (1:4)). Specifically, 70µl are spincoated at 6000 rpm (3 s acceleration step) for 35 s. After deposition of the PIL the samples were annealed at 100º C for 1 h. Afterwards, samples were transferred to an evaporation chamber and C_{60} (30 nm), BCP (8 nm) and copper (100 nm) were deposited under vacuum (p =10^{-7} mbar). The active area was 6 mm^2 defined as the overlap of ITO and the top electrode.

Mesoporous *nip* Device Preparation: FTO-coated glass (Nippon sheet glass) was chemically etched with zinc powder and HCl solution, followed by sonically cleaning using Hellmanex, water, acetone, and 2-propanol. A 30 nm thick compact TiO_2 layer was deposited by spray pyrolysis of a titanium diisopropoxide bis(acetylacetonate) solution (Sigma-Aldrich) diluted in 2-propanol (1:15 v/v) at 450 °C. A 100 nm thick mesoporous TiO_2 layer was spin coated from a solution of TiO_2 paste (GreatCellSolar, 30NR-D) in ethanol (1:8 w/v) at 5000 rpm for 20 s followed by heating at 125 °C for 10 min and sintering at 500 °C for 20 min. A thin layer of passivating tin oxide of ≈20 nm was spin-coated by using tin (IV) chloride (Acros) solution (12 µL diluted in 988 µL water) at 3000 rpm for 30 s, followed by annealing at 100 °C for 10 min and 190 °C for 1 h. The prepared substrates were treated with UV-ozone for 15 min before perovskite deposition. A 1.3M $[(FAPbI_3)_{0.87}(MAPbBr_3)_{0.13}]_{0.92}(CsPbI_3)_{0.08}$ perovskite solution with excess PbI_2 (PbI_2:FAI = 1.05:1) was prepared by mixing FAI (GreatCellSolar), MABr (GreatCellSolar), CsI (ABCR), PbI_2 (TCI), and $PbBr_2$ (TCI) in DMF and DMSO (0.78:0.22 v/v). The prepared perovskite precursor was then spin-coated on the prepared at 2000 rpm for 12 s and 5000 rpm for 30 s. Chlorobenzene was added as an anti-solvent at 15 s before the end of spin coating process. The perovskite film was heated for 1h. After cooling down to the room temperature, the PIL layer was deposited on top of the perovskite layer at 6000 rpm for 30s, then the film was subsequently annealed at 100 °C for 60 min. Spiro OMeTAD was used as the hole-transporting materials (HTM). The HTM layer was prepared by dissolving 78.2 mg spiro-OMeTAD (Borun Chemical) in 1 mL chlorobenzene doped with 31.28 µL of 4-tert-butylpyridine (Sigma-Aldrich), 18.57 µL of Li-bis (trifluoromethanesulphonyl) imide (Aldrich) from the stock solution (196 mg in 379 µL acetonitrile), 13.69 µL of FK 209 Co(III) TFSI (GreatCellSolar) from the stock solution (99 mg in 263 µL acetonitrile). The doped spiro-OMeTAD solution was then deposited by spin-coating at 4000 rpm for 30 s. Finally, a 70 nm-thick gold counter electrode was thermally evaporated on top of HTM layer.

Planar *nip* Device Preparation: Planar *n-i-p* type perovskite solar cells were prepared as a layer stack of glass/ITO/SnO_2/$Cs_{0.05}((CH(NH_2)_2)_{0.83}(CH_3NH_3)_{0.17})_{0.95}Pb(I_{0.83}Br_{0.17})_3$/HTM/Au. Patterned ITO coated glass substrates (R = 15 Ω/sq., Automatic Research) were cleaned for 15 min each with detergent, acetone and isopropanol in an ultrasonic bath and subsequently treated for 15 min in a UV/O_3 cleaner. 22.5 mg/mL $SnCl_2 \cdot 2H_2O$ was dissolved in ethanol and stirred at room temperature overnight prior to spin coating 60 µl of the solution at 1500 rpm for 30 s. In a second step, another 60 µl of the $SnCl_2$ solution were dispersed on the substrate and rotated at 2500 rpm for 30 s before annealing at 180°C for one hour. After another UV/O_3 cleaning for 15 minutes, a KNO_3 solution (2.5 mg/ml in DI-H_20) was spin-coated onto the SnO_2 layer at 4000 rpm and annealed at 120°C for 10 minutes. Further layers were deposited in a N2 filled glovebox. $Cs_{0.05}(FA_{0.83}MA_{0.17})_{0.95}Pb(I_{0.83}Br_{0.17})_3$ perovskite was prepared from a precursor solution of FAI (1 M), PbI2 (1.1 M), MABr (0.2 M) and PbBr2 (0.2 M) in anhydrous

DMF:DMSO 4:1 (v:v). Further, 5 mol-% CsI from a 1.5 M stock solution in DMSO was added to the precursor solution. The perovskite solution was spin coated in a two-step program at 1000 rpm for 10 s and 6000 rpm for 20 s. 5 s before to the end of the program, 160 µL of chlorobenzene was poured on the spinning substrate. Subsequently, the sample was annealed at 100 °C for 1 h. Next 36.2 mg of spiro-OMeTAD was dissolved in 1 mL of CBZ, 8.8 µL of a LiTFSI stock solution (520 mg/mL in acetonitrile), 14.5 µL of a FK209 stock solution (300 mg/mL in acetonitrile), and 14.4 µL of TBP. The doped spiro-OMeTAD solution was spin coated onto the samples at 1800 rpm for 30 s. Finally, 80 nm of gold were thermally evaporated at a base pressure of 10^{-6} mbar and a rate of 0.7 Å/s through shadow masks defining six active areas of 16 mm² per substrate.

Current Density–Voltage Characteristics, EQE$_{PV}$ and 2-probe conductivity: J-V curves were measured under N_2 on a Keithley 2400 system in a 2-wire configuration with a scan speed of 0.1V/s and voltage step of 0.02V. One sun illumination at approximately 100mWcm^{-2} of AM1.5G irradiation was provided by a Oriel class ABA sun simulator. The real illumination intensity was monitored during the measurement using a Si photodiode and the exact illumination intensity was used for efficiency calculations. The sun simulator was calibrated with a KG5 filtered silicon solar cell (certified by Fraunhofer ISE). The AM1.5G short-circuit current of devices matched the integrated product of the EQE spectrum within 5-10% error. The latter was recorded using a home build set-up utilizing a Philips Projection Lamp (Type7724 12 V 100 W) in front of a monochromator (Oriel Cornerstone 74100) and the light was mechanically chopped at 70 Hz. The photo-generated current was measured using a lock-in-amplifier (EG&G Princeton Applied Research Model 5302, integration times 300 ms) and evaluated after calibrating the lamp spectrum with an UV-enhanced Si photodetector (calibrated at Newport). The 2-probe conductivity was measured through current-voltage characteristics with an Agilent 4155C semiconductor parameter analyzer. The voltage was swept from positive to negative and the number of recorded points was kept at 201.

Absolute Photoluminescence: Excitation for the PL measurements was performed with a 445 nm CW laser (Insaneware) through an optical fibre into an integrating sphere. The intensity of the laser was adjusted to a 1 sun equivalent intensity by illuminating a 1 cm^2-size perovskite solar cell under short-circuit and matching the current density to the J_{SC} under the sun simulator (22.0 mA/cm^2 at 100 mWcm^{-2}, or 1.375x10^{21} photons m^{-2}s^{-1}). A second optical fiber was used from the output of the integrating sphere to an Andor SR393i-B spectrometer equipped with a silicon CCD camera (DU420A-BR-DD, iDus). The system was calibrated by using a calibrated halogen lamp with specified spectral irradiance, which was shone into to integrating sphere. A spectral correction factor was established to match the spectral output of the detector to the calibrated spectral irradiance of the lamp. The spectral photon density was obtained from the corrected detector signal (spectral irradiance) by division through the photon energy (hf), and the photon numbers of the excitation and emission obtained from numerical integration using Matlab. In a last step, three fluorescent test samples with high specified PLQY (~70%) supplied from Hamamatsu Photonics where measured where the specified value could be accurately reproduced within a small relative error of less than 5%.

Time Resolve Photoluminescence: Timeresolved PL data was acquired with a TCSPC system (Berger & Lahr) after excitation with a pulse-picked and frequency-doubled output from a mode-locked Ti:sapphire oscillator (Coherent Chameleon) with nominal pulse durations ~ 100fs and fluence of ~30nJ/cm² at a wavelength of 470nm.

Energy Disperisive X-Ray maps were acquired by means of an Oxford Instruments Ultim Extreme windowless X-ray detector in a Zeiss UltraPlus scanning electron microscope (SEM). Measurements were performed with an acceleration voltage of 3 kV and a beam current of about 10 pA.

Cathodoluminescence intensity maps were acquired by means of a Zeiss MERLIN SEM equipped with a SPARC system from Delmic. An aluminium parabolic mirror positioned above the sample focused the light into a photomultiplier tube (Thorlabs, PMT1001) outside the SEM chamber. We minimized the effect of beam damage by measuring under mild beam conditions (50 pA and 3.5 kV) and reduced electron dose (10 nm pixel size and 15 µs dwelling time per pixel).

Atomic Force Microscopy and Conductive Atomic Force Microscopy were performed with a Solver NT-MDT instrument with a hardware linearized 100 µm scanner and scanning tip. The measurements were performed in contact mode by measuring both spreading resistance and topography. The tip used was a platinum NSG10/Pt.

Contact Angle: The contact angle profile of CMB-TA on perovskite MAPI thin film were determined by droplet shape profile analysis from OCA instrument, data physics ES, Germany, and drop shape analysis dsa1 V1.80 Krüss software.

Poly-Ionic Liquid Synthesis

Materials

1-Vinylimidazole, 1-methylimidazole, ethylbromide, 4-vinylbenzyl chloride, water-soluble nonionic azo-initiator VA86 (WakeChemicals), and lithium bis(trifluoromethylsulfonyl)imide (TFSI; Aldrich 97%) were used as received without further purifications. All solvents used were of analytic grade.

IL-monomer synthesis(1-ethyl-3-vinilimidazolium bromide)

1-Vinylimidazole (4.7 g 0.05 M) were dissolved in 100 mL of methanol in a round bottom flask. Slowly addition of Ethyl bromide (6.5 g 0.06 M) while stirring further 1 hour. Then the solution was heated to 40 °C for 24 h. After the solution was cooled to room temperature, the white precipitate was washed with diethyl ether several times. Finally the precipitate was dried in a vacuum ($1*10^{-3}$ mbar) oven. (Yield 90% , 9.1 g)

Polymer synthesis

The IL monomer (5.0 g) was dissolved in deionized water (50 mL) in a round bottom flask. After the monomer was dissolved, water-soluble nonionic azo-initiator VA86 (120 mg) was added. The mixture was purged with argon for 30 minutes and then stirred and heated to 85 °C for 24 h. After cooling to room temperature, the solution was precipitated into ice cooled THF (50 mL). A beige powder was filtered off and washed several times with THF. The dry powder was dried at 80°C under vacuum for 10 h. (3.0 g, 60%).

Ionic Exchange

The anion metathesis was performed by adding an aqueous solution of Li-TFSI (5.63 g, 20 mmol) into the aqueous solution of Br contained polymer to replace Br^- by $TFSI^-$. The resulting mixture was stirred for 1 h before filtering the solution using Por. 4 Buchner filter. The polymer was washed 5 times with water and dried in vacuum oven over night at 70 °C (2.1 g, 72%).

X-ray diffraction (XRD) patterns were obtained using Bruker D8 Advance X-ray diffractometer via Cu-K_α radiation.

X-ray and ultraviolet photoemission (XPS and UPS) measurements were conducted using a JEOL (JPS-9030) photoelectron spectrometer, which is equipped with a monochromatized Al

Kα source (1486.6 eV) for XPS and hydrogen Lyman-α emission (10.2 eV) for UPS measurements.

Stability tests are carried out in N2 atmosphere keeping the device under constant illumination at AM 1.5 1 sun equivalent illumination condition. The devices utilizing BCP are measure at a temperature of 50 °C whereas the devices utilizing SnO_2 were kept at a constant temperature of 25 °C. The tracking method used is a continues maximum power point tracking algorithm.

Bibliography

1. Yin, W.-J., Shi, T. & Yan, Y. Unusual defect physics in CH 3 NH 3 PbI 3 perovskite solar cell absorber. *Appl. Phys. Lett* **104**, 063903 (2014).
2. De Wolf, S. *et al.* Organometallic halide perovskites: Sharp optical absorption edge and its relation to photovoltaic performance. *J. Phys. Chem. Lett.* **5**, 1035–1039 (2014).
3. Yin, W.-J., Yang, J.-H., Kang, J., Yan, Y. & Wei, S.-H. Halide perovskite materials for solar cells: a theoretical review. *J. Mater. Chem. A* **3**, 8926–8942 (2015).
4. Cai, M. *et al.* Cost-Performance Analysis of Perovskite Solar Modules. *Adv. Sci.* **4**, 1600269 (2017).
5. Green, M. A., Ho-Baillie, A. & Snaith, H. J. The emergence of perovskite solar cells. *Nat. Photonics* **8**, 506–514 (2014).
6. Hodes, G. Perovskite-Based Solar Cells. *Science (80-.).* **342**, 317–318 (2013).
7. Dong, Q. *et al.* Electron-hole diffusion lengths > 175 μm in solution-grown CH3NH3PbI3 single crystals. *Science (80-.).* **347**, 967–970 (2015).
8. Stranks, S. D. *et al.* Electron-Hole Diffusion Lengths Exceeding 1 Micrometer in an Organometal Trihalide Perovskite Absorber. *Science (80-.).* **342**, 341–344 (2013).
9. Braly, I. L. *et al.* Hybrid perovskite films approaching the radiative limit with over 90% photoluminescence quantum efficiency. *Nat. Photonics* **12**, 355–361 (2018).
10. Correa-Baena, J.-P. *et al.* Promises and challenges of perovskite solar cells. *Science* **358**, 739–744 (2017).
11. Tress, W. Perovskite Solar Cells on the Way to Their Radiative Efficiency Limit – Insights Into a Success Story of High Open-Circuit Voltage and Low Recombination. *Adv. Energy Mater.* **7**, 1602358 (2017).
12. Domanski, K., Alharbi, E. A., Hagfeldt, A., Grätzel, M. & Tress, W. Systematic investigation of the impact of operation conditions on the degradation behaviour of perovskite solar cells. *Nat. Energy* **3**, 61–67 (2018).
13. Noel, N. K. *et al.* Enhanced Photoluminescence and Solar Cell Performance via Lewis Base Passivation of OrganicÀInorganic Lead Halide Perovskites. **8**, 9815–9821 (2014).
14. Zheng, X. *et al.* Defect passivation in hybrid perovskite solar cells using quaternary ammonium halide anions and cations. *Nat. Energy* **2**, 17102 (2017).
15. Wolff, C. M. *et al.* Reduced Interface-Mediated Recombination for High Open-Circuit

Voltages in CH 3 NH 3 PbI 3 Solar Cells. *Adv. Mater.* **29**, 1700159 (2017).

16. Deng, W., Liang, X., Kubiak, P. S. & Cameron, P. J. Molecular Interlayers in Hybrid Perovskite Solar Cells. *Adv. Energy Mater.* **8**, 1–20 (2018).

17. Caprioglio, P. *et al.* High open circuit voltages in pin-type perovskite solar cells through strontium addition. *Sustain. Energy Fuels* **3**, 550–563 (2019).

18. Abdi-Jalebi, M. *et al.* Maximizing and stabilizing luminescence from halide perovskites with potassium passivation. *Nature* **555**, 497–501 (2018).

19. Saliba, M. *et al.* Incorporation of rubidium cations into perovskite solar cells improves photovoltaic performance. *Science (80-.).* **354**, 206–209 (2016).

20. Klug, M. T. *et al.* Tailoring metal halide perovskites through metal substitution: influence on photovoltaic and material properties. *Energy Environ. Sci.* **236**, 236–246 (2017).

21. Bi, D. *et al.* Polymer-templated nucleation and crystal growth of perovskite films for solar cells with efficiency greater than 21%. *Nat. Energy* **1**, 16142 (2016).

22. Zuo, L. *et al.* Polymer-modified halide perovskite films for efficient and stable planar heterojunction solar cells. *Sci. Adv.* **3**, e1700106 (2017).

23. Wu, Q. *et al.* Solution-Processable Ionic Liquid as an Independent or Modifying Electron Transport Layer for High-Efficiency Perovskite Solar Cells. (2016). doi:10.1021/acsami.6b12683

24. Zhang, H. *et al.* Improved High-Efficiency Perovskite Planar Heterojunction Solar Cells via Incorporation of a Polyelectrolyte Interlayer. *Chem. Mater.* **26**, 5190–5193 (2014).

25. Grancini, G. & Nazeeruddin, M. K. Dimensional tailoring of hybrid perovskites for photovoltaics. *Nat. Rev. Mater.* **4**, 4–22 (2019).

26. Cohen, B.-E. El, Wierzbowska, M. & Etgar, L. High efficiency quasi 2D lead bromide perovskite solar cells using various barrier molecules. *Sustain. Energy Fuels* **1**, 1935–1943 (2017).

27. Etgar, L. The merit of perovskite's dimensionality; can this replace the 3D halide perovskite? *Energy Environ. Sci.* **11**, 234–242 (2018).

28. Cho, K. T. *et al.* Water-Repellent Low-Dimensional Fluorous Perovskite as Interfacial Coating for 20% Efficient Solar Cells. *Nano Lett* **18**, (2018).

29. Cho, K. T. *et al.* Highly efficient perovskite solar cells with a compositionally engineered perovskite/hole transporting material interface. *Energy Environ. Sci.* **10**, 621–627 (2017).

30. Grancini, G. *et al.* One-Year stable perovskite solar cells by 2D/3D interface engineering. *Nat. Commun.* **8**, 1–8 (2017).

31. Qiao, R. & Zuo, L. Self-assembly monolayers boosting organic-inorganic halide perovskite solar cell performance. *J. Mater. Res* **33**, 387–400 (2019).

32. Chang, C.-Y. *et al.* Achieving high efficiency and improved stability in large-area ITO-free perovskite solar cells with thiol-functionalized self-assembled monolayers. *J. Mater. Chem. A* **4**, 7903–7913 (2016).

33. Al-Ashouri, A. *et al.* Conformal monolayer contacts with lossless interfaces for perovskite single junction and monolithic tandem solar cells. *Energy Environ. Sci.* **12**, 3356–3369 (2019).

34. Christians, J. A. *et al.* Tailored interfaces of unencapsulated perovskite solar cells for >1,000 hour operational stability. *Nat. Energy* **3**, 68–74 (2018).

35. Jeon, N. J. *et al.* A fluorene-terminated hole-transporting material for highly efficient and stable perovskite solar cells. *Nat. Energy* **3**, 682–689 (2018).

36. Turren-Cruz, S.-H., Hagfeldt, A. & Saliba, M. Methylammonium-free, high-performance, and stable perovskite solar cells on a planar architecture. *Science (80-.).* **362**, 449–453 (2018).

37. Seo, J.-Y. Y. *et al.* Ionic Liquid Control Crystal Growth to Enhance Planar Perovskite Solar Cells Efficiency. *Adv. Energy Mater.* **6**, 1–6 (2016).

38. Wang, J. *et al.* Halide perovskite based on hydrophobic ionic liquid for stability improving and its application in high-efficient photovoltaic cell. *Electrochim. Acta* **303**, 133–139 (2019).

39. Xia, R. *et al.* Retarding Thermal Degradation in Hybrid Perovskites by Ionic Liquid Additives. *Adv. Funct. Mater.* **29**, 1902021 (2019).

40. Bai, S. *et al.* Planar perovskite solar cells with long-term stability using ionic liquid additives. *Nature* **571**, 245–250 (2019).

41. Yang, D. *et al.* Surface optimization to eliminate hysteresis for record efficiency planar perovskite solar cells. *Energy Environ. Sci.* **9**, 3071–3078 (2016).

42. Li, M. *et al.* Interface Modification by Ionic Liquid: A Promising Candidate for Indoor Light Harvesting and Stability Improvement of Planar Perovskite Solar Cells. *Adv. Energy Mater.* **8**, 1801509 (2018).

43. Wang, S. *et al.* Water-Soluble Triazolium Ionic-Liquid-Induced Surface Self-Assembly to Enhance the Stability and Efficiency of Perovskite Solar Cells. *Adv. Funct. Mater.* 1900417 (2019). doi:10.1002/adfm.201900417

44. Ghosh, S. & Singh, T. Role of ionic liquids in organic-inorganic metal halide perovskite solar cells efficiency and stability. *Nano Energy* **63**, 103828 (2019).

45. Yuan, J. & Antonietti, M. Poly(ionic liquid)s: Polymers expanding classical property profiles. *Polymer (Guildf).* **52**, 1469–1482 (2011).

46. Spanos, I. *et al.* Poly(ionic liquid) binders as ionic conductors and polymer electrolyte interfaces for enhanced electrochemical performance of water splitting electrodes. *Sustain. Energy Fuels* **2**, 1446–1451 (2018).

47. Gao, M. R., Yuan, J. & Antonietti, M. Ionic Liquids and Poly(ionic liquid)s for Morphosynthesis of Inorganic Materials. *Chem. - A Eur. J.* **23**, 5391–5403 (2017).

48. Qian, W., Texter, J. & Yan, F. Frontiers in poly(ionic liquid)s: Syntheses and applications. *Chem. Soc. Rev.* **46**, 1124–1159 (2017).

49. Wang, S. *et al.* Polymeric room-temperature molten salt as a multifunctional additive toward highly efficient and stable inverted planar perovskite solar cells. *Energy Environ. Sci.* **13**, 5068–5079 (2020).

50. Stolterfoht, M. *et al.* Approaching the fill factor Shockley–Queisser limit in stable, dopant-free triple cation perovskite solar cells. *Energy Environ. Sci.* **10**, 1530–1539 (2017).

51. Saliba, M. *et al.* Cesium-containing Triple Cation Perovskite Solar Cells: Improved Stability, Reproducibility and High Efficiency. *Energy Environ. Sci.* **9**, 1989–1997 (2016).

52. Stolterfoht, M. *et al.* Visualization and suppression of interfacial recombination for high-efficiency large-area pin perovskite solar cells. *Nat. Energy* **3**, 847–854 (2018).

53. Würfel, U., Neher, D., Spies, A. & Albrecht, S. Impact of charge transport on current-voltage characteristics and power-conversion efficiency of organic solar cells. *Nat. Commun.* **6**, (2015).

54. Luo, D. *et al.* Enhanced photovoltage for inverted planar heterojunction perovskite solar cells. *Science (80-.).* **360**, 1442–1446 (2018).

55. Yang, S. *et al.* Tailoring Passivation Molecular Structures for Extremely Small Open-Circuit Voltage Loss in Perovskite Solar Cells. *J. Am. Chem. Soc.* **141**, 5781–5787 (2019).

56. Perdew, J. P., Burke, K. & Ernzerhof, M. Generalized gradient approximation made simple. *Phys. Rev. Lett.* **77**, 3865–3868 (1996).

57. Meggiolaro, D. *et al.* Iodine chemistry determines the defect tolerance of lead-halide perovskites. *Energy Environ. Sci.* **11**, 702–713 (2018).

58. Adamo, C. & Barone, V. Toward reliable density functional methods without adjustable parameters: The PBE0 model. *J. Chem. Phys.* **110**, 6158–6170 (1999).

59. Wang, Q. *et al.* Enhancing efficiency of perovskite solar cells by reducing defects through imidazolium cation incorporation. *Mater. Today Energy* **7**, 161–168 (2018).

60. Noel, N. K. *et al.* Enhanced Photoluminescence and Solar Cell Performance *via* Lewis Base Passivation of Organic–Inorganic Lead Halide Perovskites. *ACS Nano* **8**, 9815–9821 (2014).

61. Węcławik, M., Gągor, A., Piecha, A., Jakubas, R. & Medycki, W. Synthesis, crystal structure and phase transitions of a series of imidazolium iodides. *CrystEngComm* **15**, 5633 (2013).

62. Salado, M. *et al.* Towards Extending Solar Cell Lifetimes: Addition of a Fluorous Cation to Triple Cation-Based Perovskite Films. *ChemSusChem* **10**, 3846–3853 (2017).

63. Chen, B., Rudd, P. N., Yang, S., Yuan, Y. & Huang, J. Imperfections and their passivation in halide perovskite solar cells. *Chem. Soc. Rev.* **48**, 3842–3867 (2019).

64. Xu, J. *et al.* Perovskite-fullerene hybrid materials suppress hysteresis in planar diodes. *Nat. Commun.* **6**, 1–8 (2015).

65. Tseng, J.-K. *et al.* Interfacial polarization and layer thickness effect on electrical insulation in multilayered polysulfone/poly(vinylidene fluoride) films. *Polymer (Guildf).* **55**, 8–14 (2014).

66. Ganet, F. *et al.* Development of a smart guide wire using an electrostrictive polymer: option for steerable orientation and force feedback. *Sci. Rep.* **5**, 18593 (2016).

67. Caprioglio, P. *et al.* On the Origin of the Ideality Factor in Perovskite Solar Cells. *Adv. Energy Mater.* 2000502 (2020). doi:10.1002/aenm.202000502

68. Wolff, C. M., Caprioglio, P., Stolterfoht, M. & Neher, D. Nonradiative Recombination in Perovskite Solar Cells: The Role of Interfaces. *Adv. Mater.* **31**, 1902762 (2019).

69. Stolterfoht, M. *et al.* The impact of energy alignment and interfacial recombination on the internal and external open-circuit voltage of perovskite solar cells. *Energy Environ. Sci.* **12**, 2778–2788 (2019).

70. Kirchartz, T., Márquez, J. A., Stolterfoht, M. & Unold, T. Photoluminescence-Based Characterization of Halide Perovskites for Photovoltaics. *Adv. Energy Mater.* **10**, 1904134 (2020).

71. Caprioglio, P. *et al.* On the Relation between the Open-Circuit Voltage and Quasi-Fermi Level Splitting in Efficient Perovskite Solar Cells. *Adv. Energy Mater.* **9**, 1901631 (2019).

72. Stolterfoht, M. *et al.* The impact of energy alignment and interfacial recombination on the internal and external open-circuit voltage of perovskite solar cells. *Energy Environ. Sci.* **12**, 2778–2788 (2019).

73. Wolff, C. M. *et al.* Perfluorinated Self-Assembled Monolayers Enhance the Stability and Efficiency of Inverted Perovskite Solar Cells. *ACS Nano* acsnano.9b03268 (2020). doi:10.1021/acsnano.9b03268

74. Ahn, N. *et al.* Trapped charge-driven degradation of perovskite solar cells. *Nat. Commun.* **7**, 13422 (2016).

75. Snaith, H. J. Perovskites: The Emergence of a New Era for Low-Cost, High-Efficiency Solar Cells. *J. Phys. Chem. Lett.* **4**, 3623–3630 (2013).

76. Motti, S. G. *et al.* Controlling competing photochemical reactions stabilizes perovskite solar cells. *Nat. Photonics* (2019). doi:10.1038/s41566-019-0435-1

77. Bryant, D. *et al.* Light and oxygen induced degradation limits the operational stability of methylammonium lead triiodide perovskite solar cells. *Energy Environ. Sci.* **9**, 1655–1660 (2016).

78. Pearson, A. J. *et al.* Oxygen Degradation in Mesoporous Al2O3/CH3NH3PbI3-xClx Perovskite Solar Cells: Kinetics and Mechanisms. *Adv. Energy Mater.* **6**, 1–10 (2016).

79. Zhao, J., Wang, A., Altermatt, P. P., Wenham, S. R. & Green, M. A. 24% Efficient perl silicon solar cell: Recent improvements in high efficiency silicon cell research. *Sol. Energy Mater. Sol. Cells* **41**–**42**, 87–99 (1996).

80. Abate, A. *et al.* Protic ionic liquids as p-dopant for organic hole transporting materials and their application in high efficiency hybrid solar cells. *J. Am. Chem. Soc.* **135**, 13538–13548 (2013).

81. Gutierrez-Partida, E. *et al.* Large-Grain Double Cation Perovskites with 18 μs Lifetime and High Luminescence Yield for Efficient Inverted Perovskite Solar Cells. *Cite This ACS Energy Lett* **6**, (2021).